Improving Damped Random Walk parameters for SDSS Stripe82 Quasars with Pan-STARRS1.

Krzysztof L. Suberlak,[1] Željko Ivezić,[1] and Chelsea MacLeod[2]

[1] Department of Astronomy
University of Washington
Seattle, WA 98195, USA
[2] Harvard Smithsonian Center for Astrophysics
60 Garden St, Cambridge, MA 02138, USA

ABSTRACT

We use the Panoramic Survey Telescope and Rapid Response System 1 Survey (Pan-STARRS1, PS1) data to extend the Sloan Digital Sky Survey (SDSS) Stripe 82 quasar light curves. Combining PS1 gri and SDSS r light curves provides 15 years baseline for 9248 quasars, improving on previous studies using SDSS data only. We fit the light curves with Damped Random Walk (DRW) model, and correlate the DRW parameters - asymptotic variability amplitude SF_{∞}, and characteristic timescale τ, with quasar physical properties - black hole mass, bolometric luminosity, and redshift. We find that compared to other studies the characteristic timescale τ is more strongly dependent on quasar luminosity, and has a weaker dependence on the black hole mass. The variability amplitude is less strongly dependent on the quasar luminosity. We make predictions on fidelity of DRW retrieval once ZTF and LSST data become available.

1. INTRODUCTION

Quasars are variable at the rms level of 0.2 mag. They are distant active galactic nuclei, harboring a supermassive black hole surrounded by a hot accretion disk. Although it is agreed upon that the thermal emission from the accretion disk is the source of the majority of optical light, the detailed origin of variability has been debated for the past 50 years (Sun et al. 2018 and references therein). Some favor a thermal origin of variability (Kelly et al. 2013), related to the propagation of inhomogeneities ("hot spots") in the disk (Dexter & Agol 2011; Cai et al. 2016), others suggested magnetically elevated disks (Dexter & Begelman 2019), or X-ray reprocessing (Kubota & Done 2018). Indeed, it may well be that the answer involves combination of these - as Sánchez-Sáez et al. (2018) suggests, perhaps short-term variability (hours-days) is linked to the changes in X-ray flux, while long-term variability (months-years) is more intrinsic to the disk (Edelson et al. 2015; Lira et al. 2015). Nevertheless, quasar light curves have been

Corresponding author: Krzysztof Suberlak
suberlak@uw.edu

successfully described using the Damped Random Walk (DRW) model (Kelly et al. 2009; MacLeod et al. 2010; Kozłowski et al. 2010; Zu et al. 2011; Kasliwal et al. 2015), and the DRW parameters have been linked to the physical quasar properties (MacLeod et al. 2010 , hereafter M10).

Variability is also a classification tool, allowing to distinguish quasars from other variable sources that do not exhibit a stochastic variability pattern (MacLeod et al. 2011). This property is especially useful for selecting quasars in the intermediate redshift range, which overlaps the stellar locus in color-color diagrams (Sesar et al. 2007; Yang et al. 2017)). Variability has also been used to increase the completeness in measurements of Quasar Luminosity Function (see Ross et al. 2013; Palanque-Delabrouille et al. 2013; AlSayyad 2016; McGreer et al. 2013, 2018).

Due to its stochastic nature, the DRW process requires the light curve to be several times longer than the characteristic timescale for an unbiased parameter retrieval (Kozłowski et al. 2010; Kozłowski, Szymon 2017, hereafter K17). For this reason, some studies have restricted the probed redshift range, limiting the quasar sample to where one would expect only shorter timescales based on previous studies (Sun et al. 2018; Guo et al. 2017),

some have elected not to study timescales at all (Sun et al. 2018; Sánchez-Sáez et al. 2018), while others have suffered from short-baseline biases by employing single-survey data (Hernitschek et al. 2016).

In this study by extending available quasar light curves we are able to better recover a wider range of DRW timescales, and probe a wider range of redshifts and black hole masses. Almost a decade ago M10 published their research using SDSS Stripe 82 data, and new datasets (PS1,PTF,CRTS) have become available since, that can extend the quasar light curves by almost 50% . Indeed, Li et al. (2018) combined SDSS and Dark Energy Camera Legacy Survey (DECaLS) data, to provide a 15 year baseline, but by focusing on a large area to encompass as many quasars as possible (119,305 up to z=4.89) suffered from poor sampling which lends itself better to an ensemble structure function approach rather than direct light curve modeling. On the other hand, Sánchez-Sáez et al. (2018) who employed optical data from QUEST-La Silla AGN variability survey, also used the Structure Function parametrization (amplitude of variability and the excess variance), because the light curve length (less than 5 years for 2435 quasars) excluded the possibility of unbiased retrieval of characteristic timescale. A different parameter space of cadence and baseline was explored by Kepler-based studies, with extremely well-sampled light curves (30 min cadence) of a small number of quasars, with baselines of up to 4 years (Mushotzky et al. 2011; Edelson et al. 2014; Kasliwal et al. 2015, 2017; Smith et al. 2018; Aranzana et al. 2018). Finally other studies suffered from restricted quasar samples to avoid aforementioned biases (Guo et al. 2017; Sun et al. 2018), or small number of objects satisfying their cuts (Kelly et al. 2009; Kelly et al. 2013; Simm et al. 2016). There were also those who studied quasar variability with the ensemble structure function approach, which works well if only a small number of epochs is available per object, but it lacks the appeal of a direct object-by-object modeling (Bauer et al. 2009; MacLeod et al. 2012; Caplar et al. 2017; Kozłowski 2016)

Unlike previous studies, in this work, by combining SDSS and PS1 data we afford both an extended baseline (15 years), and a large number (9000) of quasars to which we fit the DRW model. First we confirm in Section 2 that extending the quasar baseline is the most important improvement in providing unbiased estimates of the DRW model parameters (K17). In Section 3 we describe the datasets employed, and their combination onto a common photometric system. In Section 4 we test the improvement in DRW parameters with simulation. Finally in Section 5 we describe the main results

analyzing correlations between physical parameters and variability, and in Section 6 we summarize the main results. In this work we adopt a ΛCDM cosmology with $h_0 = 0.7$ and $\Omega_m = 0.3$.

2. METHODS

2.1. *DRW as a Gaussian Process*

Damped Random Walk (Ornstein-Uhlenbeck process) can be modeled as a member of a class of Gaussian Processes (GP). Each GP is described by a mean and a kernel - a covariance function that contains a measure of correlation between two points: x_n and x_m, separated by Δt_{nm} (autocorrelation). For the DRW process, the covariance between two observations spaced by Δt_{nm} is:

$$
\begin{aligned}
k(\Delta t_{nm}) &= a \exp\left(-\Delta t_{tm}/\tau\right) \\
&= \sigma^2 \exp\left(-\Delta t_{tm}/\tau\right) \\
&= \sigma^2 ACF(\Delta t_{tm})
\end{aligned}
\tag{1}
$$

Here a or σ^2 is an amplitude of correlation decay as a function of Δt_{tm}, while τ is the characteristic timescale over which correlation drops by $1/e$. For a DRW, the correlation function $k(\Delta t_{nm})$ is also related to the autocorrelation function ACF.

Not explicitly used in this paper, but of direct relevance to the DRW modeling, is the structure function (SF). SF can be found from the data as the root-mean-squared of magnitude differences Δm calculated as a function of temporal separation Δt (we drop subscripts n,m for brevity). SF is directly related to a DRW kernel $k(\Delta t)$:

$$
SF(\Delta t) = SF_\infty (1 - \exp\left(-|\Delta t|/\tau\right))^{1/2}
\tag{2}
$$

For quasars SF follows approximately a power law: $SF \propto \Delta t^\beta$, and it levels out for large time lags Δt to a constant value of SF_∞. Note that $SF_\infty = \sqrt{2}\sigma$ in the above (also see MacLeod et al. (2012); Bauer et al. (2009); Graham et al. (2015) for an overview).

The likelihood for the particular value of DRW parameters given the data is evaluated with celerite (Foreman-Mackey et al. 2017) - a fast GP solver that scales linearly with the number of data points $\mathcal{O}(N)$ thanks to an optimization that exploits the structure of covariance matrix for kernels that are a mixture of exponentials, such as a DRW kernel (Foreman-Mackey et al. 2018; Ambikasaran et al. 2015). The method employed is similar to that used by Rybicki & Press (1992); Kozłowski et al. (2010), M10 - like in previous work, we use a uniform prior in log space on DRW fit parameters. The main difference in our approach is that rather than adopting the Maximum A-Posteriori (MAP) as the 'best-fit' value for

the DRW parameters (as done in Kozłowski et al. 2010, K17, Kozłowski 2016, M10, MacLeod et al. 2011), we find the expectation value of the marginalized log posterior. This is advantageous because of a non-Gaussian shape of the log posterior - it if were described by a 2D Gaussian, then the expectation value would coincide with the maximum of the log posterior.

2.2. *The impact of light curve baseline*

K17 reports that one cannot trust any results of DRW fitting unless the light curve length is at least ten times longer than the characteristic timescale. We confirm these generic trends, although we find that the stringent requirements of K17 can be somewhat relaxed. Following K17 setup, we model 10 000 DRW light curves with fixed length (baseline) $t_{exp} = 8$ years, asymptotic variability amplitude of $SF_\infty = 0.2$ mag, SDSS or OGLE-like cadence, sampling over a range of input timescales. With fixed baseline, this spans the parameter space of $\rho = \tau/t_{exp}$, $\rho \in \{0.01 : 15\}$. We simulate 100 light curves at each ρ.

The true underlying DRW signal $s(t)$ is found by iterating over the array of time steps t. At each step, we draw a point from a Gaussian distribution, for which the mean and standard deviation are re-calculated at each timestep (see Kelly et al. 2009 (eqs. A4 and A5) as well as in MacLeod et al. (2010) (Sec. 2.2), and K17). Starting at t_0, the signal is equal to the mean magnitude, $s_0 = \langle m \rangle$. After a timestep $\Delta t_i = t_{i+1} - t_i$, the signal s_{i+1} is drawn from $\mathcal{N}(loc, stdev)$, with :

$$loc = s_i e^{-r} + \langle m \rangle \left(1 - e^{-r}\right) \qquad (3)$$

and

$$stdev^2 = 0.5\, SF_\infty^2 \left(1 - e^{-2r}\right) \qquad (4)$$

where $r = \Delta t_i/\tau$, and τ is the damping timescale.

To simulate observational conditions we add to the true underlying signal $s(t)$ a noise offset, $n(t)$. Like K17, we assume $n(t)$ to be drawn from a Gaussian distribution $\mathcal{N}(0, \sigma(t))$ with a width $\sigma(t)$, corresponding to the photometric uncertainty at the given epoch:

$$y(t) = s(t) + n(t) \qquad (5)$$

We adopt SDSS S82-like cadence with N=60 epochs, or OGLE-III like cadence with N=445 epochs. The errors are set by the adopted mean magnitudes, $r = 17$ and $I = 18$:

$$\sigma_{SDSS}^2 = 0.013^2 + \exp\left(2(r - 23.36)\right) \qquad (6)$$

$$\sigma_{OGLE}^2 = 0.004^2 + \exp\left(1.63(I - 22.55)\right) \qquad (7)$$

Fig. 1 shows the recovered ρ_{out} as a function of input ρ_{in}. This confirms the findings of K17: the recovered ρ becomes meaningless ('unconstrained') if the available DRW light curve baseline is not at least several times longer than the input timescale ($\log_{10}(\rho) \lesssim -0.5$, i.e. $\rho \lesssim 3$). Consequently, by extending the baseline we can move from the biased region (bottom left) to the unbiased regime (top right). This is the basis for this study, in which we extend the baselines of quasar light curves from SDSS-only (10 years) to combined SDSS-PS1 (15 years).

2.3. *Departure from DRW?*

The power spectral density (PSD) of the DRW process is:

$$P(f) = \frac{4\sigma^2\tau}{1 + (2\pi\tau f)^2} \qquad (8)$$

(with $\sigma = SF_\infty/\sqrt{2}$, τ the characteristic timescale, f the frequency), so that $P(f) \propto f^{-2}$ at high frequencies $f > (2\pi\tau)^{-1}$, and levels to a constant value at lower frequencies(Kelly et al. 2014). This can be parametrized as $\log(P(f)) \propto \alpha_h \log(f)$ at high frequencies (short timescales), and $\log(P(f)) \propto \alpha_l \log(f)$ at low frequencies (long timescales), so that for a pure DRW process $\alpha_h = -2$ and $\alpha_l = 0$.

Various answers exist about the exact value of α_l and α_h for accurate description of quasar variability, or more broadly speaking - AGN variability.

One set of answers come from studying optical light curves of wide-field, ground-based photometric surveys, such as OGLE, SDSS, or PS1. In general, these studies used light curves with rather sparse non-uniform sampling, cadence of a few epochs per week, and overall length (baseline) of the order of several years. For instance, Zu et al. (2013) using 223 I-band OGLE quasar light curves (baseline of ~7 years, ~570 epochs) considered whether different covariance functions (powered-exponential, Matèrn, Kepler-exponential, Pareto exponential - see Eqs.5-9 in Zu et al. 2013) may present a better fit, and found that while there may be small deviations, they are not significant enough to depart from a robust DRW description. Similarly, Sun et al. (2018) found that the data quality of SDSS-like light curves was insufficient to distinguish between CAR(1) and more complex models. For the longer timescales, Guo et al. (2017) with a low-redshift subset of SDSS S82 quasars claimed that the low-frequency slope α_l should not be steeper than -1.3. For the same SDSS S82 quasars, K17 (as well as Kozłowski 2016 and Caplar et al. 2017) found PSD slopes $\alpha_h \leqslant -2$, which meant that models assuming a DRW $\alpha_h = 2$ would result in decorrelation
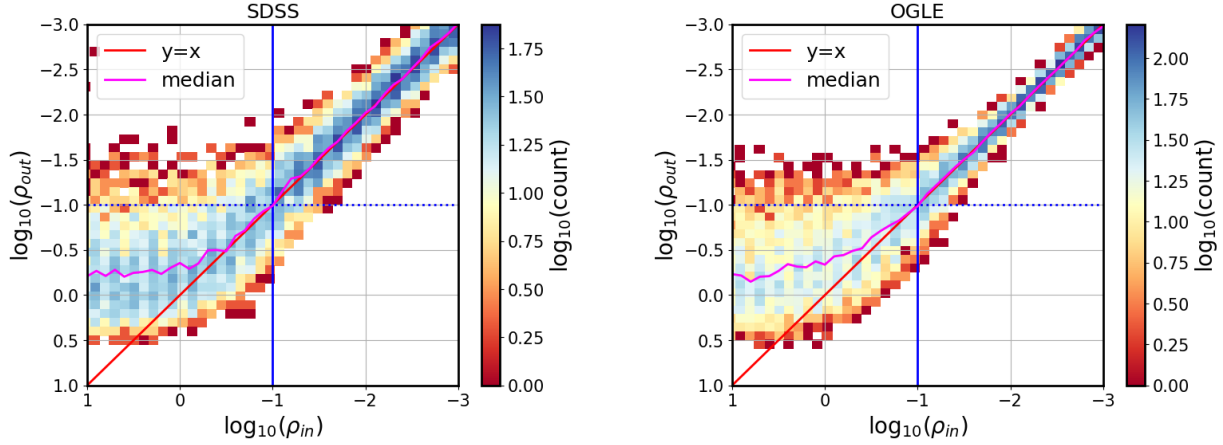
Figure 1. Probing the parameter space of $\rho = \tau/t_{exp}$, with a simulation of 10 000 light curves : 100 light curves per each of 100 ρ values spaced uniformly in logarithmic space between $\rho \in \{0.01 : 15\}$. With a baseline t_{exp} set to 8 years, we sample a range of 100 input timescales. Left panel shows the SDSS-like cadence with N=60 epochs, and the right panel the OGLE-like cadence with N=445 epochs. The dotted horizontal and solid vertical lines represent $\rho = 0.1$, i.e. the baseline is ten times longer than considered timescale. The diagonal line is $y = x$, i.e. the line that would be followed if the recovered ρ (τ) was exactly the same as the input ρ (τ). Given a quasar light curve, which has one true underlying DRW timescale, as we extend the baseline, we move from the bottom-left (unconstrained) to the top-right (well-constrained) part of the parameter space.

timescales biased low. He stated that it is currently not possible to distinguish between close-to-DRW and DRW processes for the S82 quasars because good sampling at both low frequencies (long timescales, white noise part), and high frequencies (short timescales, red / pink noise part) is not available. However, Simm et al. (2016) used a limited PS1 sample of 90 X-ray selected AGN, and with PS1 data found that their data can be described by a broken power law with low-frequency slope of -1 and high frequency slope from -2 to -4, with a break at timescale between 200 to 300 days.

A second set of answers comes from studying data with excellent cadence but short baselines from a space based Kepler mission (Borucki et al. 2010). Using Kepler light curves with a half-hour cadence enabled an unprecedented view of the high-frequency part of the AGN spectrum, but the results are inconclusive. Mushotzky et al. (2011) analyzed the four AGN light curves from 2010-2011 (three separate quarters), and found evidence of steeper slopes ($\alpha_h \sim -2.6$ to -3.1). Later, Edelson et al. (2014) combined 3.4 yrs worth of data (13 quarters) for an AGN Zw 229-15, and found the slope increasing from $\alpha_h \sim -2$ to -4 at frequency corresponding to $\Delta t = 5$ days. Smith et al. (2018) used 4 years of Kepler data for 21 AGN, and found slopes generally steeper than the DRW, between $\alpha_h \sim -2$ and -3.4 . They also concluded that, in accordance with Caplar et al. (2017), perhaps AGN are described by a combination of DRW behavior, and a changing PSD, tied to an accretion duty cycle. With the original Kepler mission ending in 2013 with the failure of the second reaction wheel, it transi-

tioned to K2, pointing at various fields around the ecliptic, which limits further the available baseline for AGN study. Aranzana et al. (2018) conducted the most extensive study of K2 AGN light curves to date, including 252 well-sampled AGN. Using data spanning 80 days they find a range of high-frequency slopes from $\alpha_h \sim -1$ to -3.2, with the median of $\alpha_h \sim -2.2$, consistent with the DRW model.

The exact shape of quasar PSD would affect other areas of study. One example is reverberation mapping (RM), which was used to provide accurate black hole mass estimates. RM is based on measuring the lags between light curves observed at different wavelengths. The two most widely used approaches to measuring interband lags are interpolated cross-correlation function (ICCF, Gaskell & Peterson 1987; Peterson et al. 2004) and light curve modeling via Markov chain Monte Carlo approach (JAVELIN, Zu et al. 2011). The PSD of the DRW comes explicitly in the latter, which assumes that the higher energies drive lower energies (whether due to x-ray reprocessing or other mechanism), and that the driving light curve is well-modeled by a DRW (with PSD equal to -2 or flatter). In this scenario other light curves (at longer wavelength) are related to it via transfer function Edelson et al. (2019). Using a wrong PSD means at best that errors are underestimated. Therefore a convincing detection of a departure of quasar PSD from that of the DRW would have a direct impact on RM studies that use JAVELIN or other light curve modeling tools.

In the end, we follow the direction laid out in M10, Sec.4.4, which shows that while within S82 sampling assuming $\alpha_h = 2$ it is impossible to reliably distinguish between a $\alpha_l = 0$ and -1. A future study with appropriate cadence would be necessary to model each quasar individually with different α_l and α_h. We elect to use the DRW description ($\alpha_l = 0$, $\alpha_h = -2$) to allow a better comparison of our results with M10.

3. DATA

3.1. Surveys

We focus on the data pertaining to a 290 deg^2 region of southern sky, repeatedly observed by the Sloan Digital Sky Survey (SDSS) between 1998 and 2008. Originally aimed at supernova discovery, objects in this area, known as Stripe82 (S82), were re-observed on average 60 times (see MacLeod et al. 2012, Sec. 2.2 for overview, and Annis et al. 2014 for details). Availability of well-calibrated (Ivezić et al. 2007), long-baseline light curves spurred variability research (see Sesar et al. 2007). The catalog prepared by Schneider et al. (2008) as part of DR9 contains 9258 spectroscopically confirmed quasars.

We extend SDSS light curves with PanSTARRS (PS1) (Chambers 2011; Flewelling 2018), Catalina Real-Time Transient Survey (CRTS) (Drake et al. 2009), and Palomar Transient Factory (PTF) (Rau et al. 2009) data. Of 9258 SDSS quasars, within $0.5''$ there are 9248 PS1 matches, 6455 PTF matches, and 7737 CRTS matches. Of these, 6444 quasars have coverage in all surveys (SDSS-PS1-PTF-CRTS). Fig 2 depicts the baseline coverage of various surveys. Each survey uses a unique set of bandpasses and cadences: SDSS light curves contain near-simultaneous $\{u, g, r, i, z\}_{\mathrm{SDSS}}$, and PS1, PTF observations in different filters are non-simultaneous.

3.2. Photometric offsets

We combine quasar photometry into a single 'master' bandpass. We choose r_{SDSS} as the target bandpass since it has the best photometry, and we calculate color terms that afford transformation from other photometric systems to SDSS. We translate to r_{SDSS} only photometry from nearby filters: $\{g, R\}_{\mathrm{PTF}}$, $\{g, r, i\}_{\mathrm{PS1}}$, V_{CRTS}.

Color terms are derived using the SDSS standard stars catalog (Ivezić et al. 2007). We focus on a 10% subset of randomly chosen stars from the catalog, and find CRTS (B.Sesar, priv.comm.), PS1 (from MAST http://panstarrs.stsci.edu) and PTF (IRSA PTF Object Catalog https://irsa.ipac.caltech.edu/) matches.

We consider the difference between the target (SDSS) and source (eg.PS1) photometry as a function of the mean SDSS $(g - i)$ color :

Table 1. Color terms (offsets) between CRTS, PTF, PS1 passbands used in combined light curves, and SDSS, using the mean $(g-i)_{\mathrm{SDSS}}$ color to spread the stellar locus. Thus the r_{SDSS} synthetic magnitude (r_s for short) can be found as $r_s = x - B_0 - B_1(g-i)_{\mathrm{SDSS}}$. This linear trend is illustrated on Fig.4, where we plot $(x - r_{\mathrm{SDSS}})$ as a function of $(g - i)_{\mathrm{SDSS}}$ for $x = g_{\mathrm{P1}}, r_{\mathrm{P1}}, i_{\mathrm{P1}}$.

Band (x)	B_0	B_1
CRTS V	-0.0464	-0.0128
PTF g	-0.0294	0.6404
PTF R	0.0058	-0.1019
PS1 g	0.0194	0.6207
PS1 r	0.0057	-0.0014
PS1 i	0.0247	-0.2765

NOTE—To derive the color terms we used SDSS S82 standard stars catalog (Ivezić et al. 2007). We randomly selected 10% of that catalog, for which 48250 have CRTS light curves. We obtained PS1 photometry from MAST, and PTF from IRSA PTF Object Catalog. We imposed quality cuts requiring that the stars are bright: $r < 19$.

$$m_{\mathrm{PS1}} - m_{\mathrm{SDSS}} = f(g - i) \qquad (9)$$

While Tonry et al. (2012) chose to spread the stellar locus with $(g-r)$ color, we prefer to use the $(g-i)$ color since it provides a larger wavelength baseline. Some authors (eg. Li et al. (2018)) allow the transformation to be a higher-order polynomial, but since we are limited to the narrow region of $(g-i)$ space occupied by quasars, before the stellar locus bend (Fig. 3), we find that the linear fit is sufficient (see Fig. 4). We summarize the resulting offsets to SDSS in Table 1.

4. SIMULATIONS : LESSONS LEARNED

We simulate the theoretical improvement of the DRW parameter retrieval in extended light curves. We generate long and well-sampled light curves, all with input $\tau = 575$ days, $SF_\infty = 0.2$ mag (the median of S82 distribution in M10). Then we subsample at SDSS, SDSS-

Figure 2. An illustration of survey baseline, sky area covered, and depth. The width of each rectangle corresponds to the extent of light curves available (or simulated) for Stripe 82 quasars for each survey. For SDSS this means DR7; for CRTS DR2, PS1 DR2, PTF DR2, ZTF year 2018, and LSST the full 10-year survey. The lower edge of each rectangle corresponds to the 5σ limiting magnitude (SDSS r, PS1 r, PTF R, ZTF r, LSST r, CRTS V). The vertical extent corresponds to the total survey area (for SDSS, up to and including DR15). Note how PS1 and PTF extend the baseline of SDSS by approximately 50%, and how inclusion of LSST triples the SDSS baseline. For reference, the area covered by LSST is 25000 sq.deg., which corresponds to 60% of the sky. The whole sky has an area of 4π steradians (41253 sq.deg.).

PS1, and predicted ZTF and LSST cadence (see Fig. 5). For the LSST 10-year segment (final LSST DR10 in 2031) we assumed 50 epochs per year, randomly distributed throughout the year, with the following error model:

$$\sigma_{LSST}(m)^2 = \sigma_{sys}^2 + \sigma_{rand}^2 \text{ (mag)}^2 \qquad (10)$$
$$\sigma_{rand}^2 = (0.04 - \gamma)x + \gamma x^2$$
$$x = 10^{0.4(m-m_5)}$$

with $\sigma_{sys} = 0.005$, $\gamma = 0.039$, $m_5 = 24.7$ (see Ivezić et al. (2019), Sec.3.2). For the ZTF 1-year segment (Spring 2019 ZTF DR1 includes data from 2018) we assumed 120 observations (every three nights) in g_{ZTF} and r_{ZTF}, deriving the magnitude-dependent error model by plotting for ZTF standard stars on Fig. 6 best mag rms as a function of best median magnitude. We find that the LSST error model (Eq. 10) with $\gamma = 0.05$, $\sigma_{sys} = 0.05$, and $m_5 = 20.8$ adequately describes the ZTF photometric uncertainty.

To mirror observational conditions we add to the true underlying DRW signal a Gaussian noise, with variance defined by photometric uncertainties for corresponding surveys. Given the noise properties of each survey (Fig. 7), we found that relatively large uncertainties of CRTS and PTF segments introduced less improvement

in recovery of DRW parameters, given that similar baseline is already covered by the PS1 data (Fig. 2). We further found that inclusion of ZTF data for 2018 would not significantly change our results. Inclusion of PS1 data with its excellent photometry (as compared to ZTF or PTF) is the best improvement over existing SDSS results. In the future (after more data has been assembled and re-calibrated) ZTF will help, but not as dramatically as LSST (see Figs. 8 and 9). For this reason we found that using only SDSS-PS1 portion is the best tradeoff between adding more baseline vs introducing more uncertainty with noisy data.

5. RESULTS: VARIABILITY PARAMETERS FOR S82 QUASARS

We extend Stripe82 quasar light curves by combining the SDSS r-band data with the PS1 g_{PS1}, r_{PS1}, i_{PS1} transformed into SDSS r-band. We fit the light curves with celerite DRW model for each quasar using either the SDSS or both SDSS and PS1 components. This yields two sets of DRW parameters per quasar: $(\tau_{SDSS}, \text{SF}_{\infty,SDSS})$, and $(\tau_{SDSS-PS1}, \text{SF}_{\infty,SDSS-PS1})$. Because the variability is inherent to the quasar, for the remaining analysis we shift all timescales to quasar rest frame, and implicitly assume that the DRW timescales are considered in rest frame: $\tau_{RF} = \tau_{OBS}/(1 + z)$.

Figure 3. Regions of color-color (upper left, upper right, bottom left), and color-magnitude (bottom right) space occupied by SDSS S82 quasars (color) and stars (contours). We use quasar median photometry from Schneider et al. (2010), and standard stars catalog of Ivezić et al. (2007), showing a random subset of 10 000 stars. We find the SDSS-PS1 color terms using the region of SDSS color space that best represents quasars, that are generally bluer than the stellar locus: $-0.5 < (g - i) < 1$. Quasars also overlap other variable sources (eg. RR Lyrae), not shown here (Sesar et al. 2007).

Figure 4. The SDSS-PS1 offsets, derived from the SDSS standard stars catalog (Ivezić et al. 2007). From randomly chosen subset of 50 000 stars, we selected only 23 000 that are sufficiently bright ($r_{SDSS} < 19$) to minimize scatter due to photometric uncertainty. On each panel we plot 20 000 SDSS stars that have PS1 match within 0.1 arcsec. Vertical dashed lines mark the region in the SDSS color space occupied by quasars (see Fig. 3), used to fit the stellar locus with a first order polynomial, marked by the solid red line.
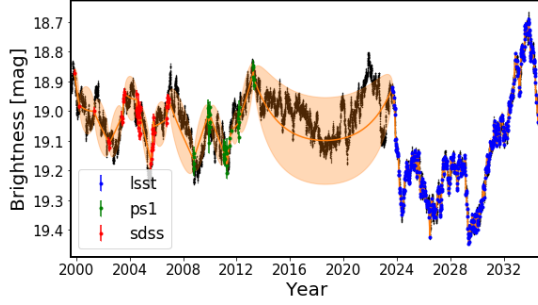
Figure 5. Simulated underlying DRW process shown here in black ($\tau = 575$d, $SF_\infty = 0.2$ mag, 4 points per day) subsampled at the real cadence of SDSS (red), PS1 (green) segments, and simulated LSST (blue) epochs, using time stamps from the combined SDSS-PS1 light curve for quasar dbID=3537034. The orange 'error snake' is an envelope marking the standard deviation of the fit to the data using a Gaussian process with DRW kernel (Sec. 4).
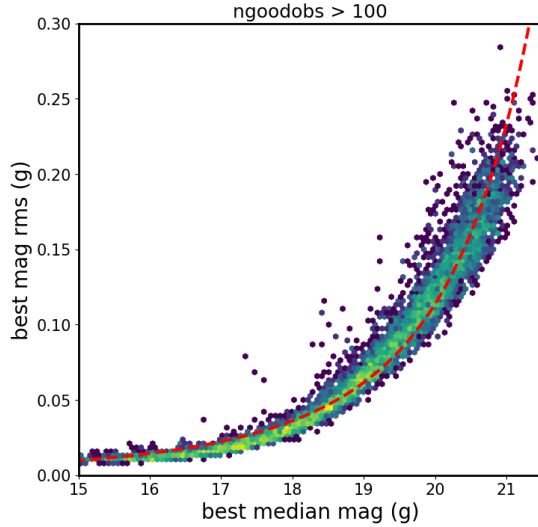
Figure 6. The best mag rms plotted as a function of magnitude for ZTF non-variable stars with over 100 observations. We overplot the adopted error model, with $\gamma = 0.05$, $\sigma_{sys} = 0.05$, and $m_5 = 20.8$ (after Ivezić et al. 2019). Properties of ZTF photometric uncertainties are largely similar to the PTF uncertainties.

In this section we first correct fitted τ, SF_∞ for wavelength dependence. Then we show the consistency with M10 results, and consider the trends between DRW parameters and physical quasar properties: black hole mass $M_{\rm BH}$, absolute i-band magnitude M_i, or redshift z.

5.1. *Comparison to M10*

As this work is based on extending the SDSS light curves (studied by M10) with the PS1 data, we directly compare the results to M10. The DRW parameters re-
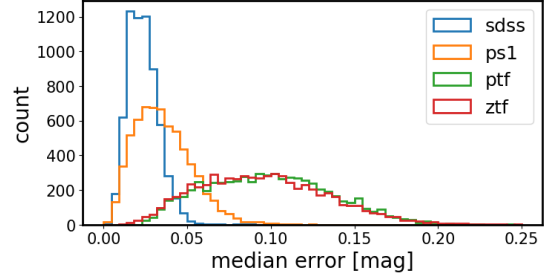
Figure 7. Distribution of median photometric uncertainties ('errors') in combined r-band real light curves. This shows that the PTF and ZTF segments have much larger errors than SDSS, PS1. This is the reason for using only SDSS-PS1 part of the combined light curve.

covered with celerite are broadly consistent - Fig. 10 shows the rest-frame τ, and SF_∞ distributions for our results for the SDSS segment (blue dashed line), SDSS-PS1 combined light curves (green dot-dashed line), and M10 SDSS for r-band only (red solid line). When using the same data as M10 (SDSS), our results agree. A detailed object-by-object comparison on Fig. 11 reveals a slight offset between log-ratios of DRW parameters, which can be attibuted to software differences.

5.2. *Rest-frame Wavelength Correction*

Since quasars are located at non-negligible redshifts, the observed wavelengths (eg. through the SDSS bandpass) probe a region of shorter wavelengths in emitted spectrum, depending on the redshift (see Shen et al. 2018, Fig.7): $\lambda_{obs} = \lambda_{RF}(1 + z)$. Thus to compare variability of the same parts of the rest-frame spectrum, we need to estimate the rest-frame emission wavelength λ_{RF}, and correct for the dependence of τ, SF_∞ on λ_{RF}. Since in this study we only used r-band light curves, we plot our SDSS and SDSS-PS1 results against M10 for SDSS ugriz, assuming for λ_{obs} the center wavelength of each SDSS bandpass (3520, 4800, 6250, 7690, 9110 Å for $ugriz$, respectively), $\lambda_{RF} = \lambda_{obs}/(1 + z)$ (using quasar redshift from Schneider et al. 2010). Fig. 12 shows τ, SF_∞ as a function of λ_{RF}. A power law dependency:

$$f \propto \left(\frac{\lambda_{RF}}{4000\text{Å}} \right)^B \tag{11}$$

describes the relationship well (solid red line on each panel). Therefore we use the same coefficients as M10: $B = -0.479$ and 0.17 for SF_∞ and τ, respectively.

5.3. *Quasar Properties: Black Hole Mass, Absolute Luminosity*

It is difficult to measure the mass of black holes living in the centers of active galaxies, even provided a

Figure 8. The ratio of DRW parameters fitted with celerite: τ and σ, to the input $\tau_{in} = 575d$, $\sigma_{in} = 0.2/\sqrt{2} \sim 0.14$ ($SF_{\infty} = 0.2$ mag). Each line corresponds to different segment of the combined SDSS-PS1-ZTF-LSST light curve. Extending the baseline by adding more data to each simulated quasar light curve allows to recover better the input parameters. The improvement with first year of ZTF data is not as large as with LSST, due to significant baseline increase compared to SDSS-PS1 (see Fig. 2). For each of the 9258 simulated light curves we employ real SDSS-PS1 cadence and photometric uncertainties (adding a Gaussian offset to the ideal underlying DRW signal), and simulated ZTF and LSST cadence and uncertainties based on the appropriate error model (see Sec. 4)

detailed spectrum. The most common approach to estimate black hole masses in AGN is to assume that the broad-line region (BLR) is virialized:

$$M_{BH} = f \frac{R\Delta V^2}{G} = f M_{vir} \qquad (12)$$

where f is a constant of order unity, R is the size of the BLR (estimated from emission-line lag Δt as $R = c\Delta t$), ΔV is virial velocity, G gravitational constant (Shen et al. 2008). From reverberation mapping studies (eg. Shen et al. 2018) we know that continuum luminosity L is related to the size of the BLR region as $R \propto L^\gamma$ (Vestergaard & Peterson 2006), with γ very close to $1/2$ (eg. Bentz et al. 2009 finds from RM studies $\gamma = 0.519 \pm 0.06$). Thus we find that $R\Delta V^2 \propto L^\gamma \Delta V^2 \equiv \mu$. The virial velocity ΔV is usually estimated from the width of the broad emission lines (or line dispersion). In the absence of a quasar spectrum, there are alternative methods using a conversion of the broad-band photometry into monochromatic fluxes in the vicinity of reverberating lines (eg. Kozłowski 2015, used in Kozłowski 2017 to estimate black hole mass for 280 000 AGN). Depending on the redshift, different rest-frame calibrated emission lines shift into the observed passband: broad Hα at 6562Å, Hβ at 5100Å, Mg II at 3000Å, and C IV at 1350Å (see Fig.7 in Shen et al. 2018, and Vestergaard 2002). Some authors even consider separately C IV-based and Mg II-based black hole mass estimates. We refer the reader to Shen et al. (2008) who in

detail describes various biases and inherent assumptions of virial black hole mass measurements.

Another important quasar property - bolometric luminosity, is most often estimated from the absolute i-band magnitude, M_i (see Shen et al. 2008, Fig.2). M_i is derived from the observed i-band magnitude, by correcting for Galactic extinction, and correcting for the fact that at different redshifts different portions of the spectral energy distribution are observed by the telescope filter bandpass. The latter, known as K-correction $K(z)$ (Oke & Sandage 1968), is defined as $m_{intrinsic} = m_{observed} - K(z)$. In the early 2000's the common approach was to K-correct to redshift 0, but as (Richards et al. 2006) pointed out, since the distribution of quasars peaks at redshift 2, for most quasars correcting to the redshift of 0 required shifting the observed spectrum into the far infrared. Moreover, the procedure was to correct separately for the continuum and emission line contributions, assuming a particular spectral shape (eg. power law $f_\nu \propto \nu^\alpha$, with $\alpha = -0.5$ - see Schneider et al. 2010; Vanden Berk et al. 2001; Richards et al. 2006). This introduces a larger error for K(z=0) than for K(z=2) if the assumed spectral shape $\alpha = -0.5$ is far from the real spectral index. In early 2010's, after Richards et al. 2006; Wisotzki 2000; Blanton et al. 2003, the practice started shifting towards K-correcting to redshift 2, and including custom qusasar spectral shapes, as reflected by the content of Shen et al. (2011) quasar catalog. Thus
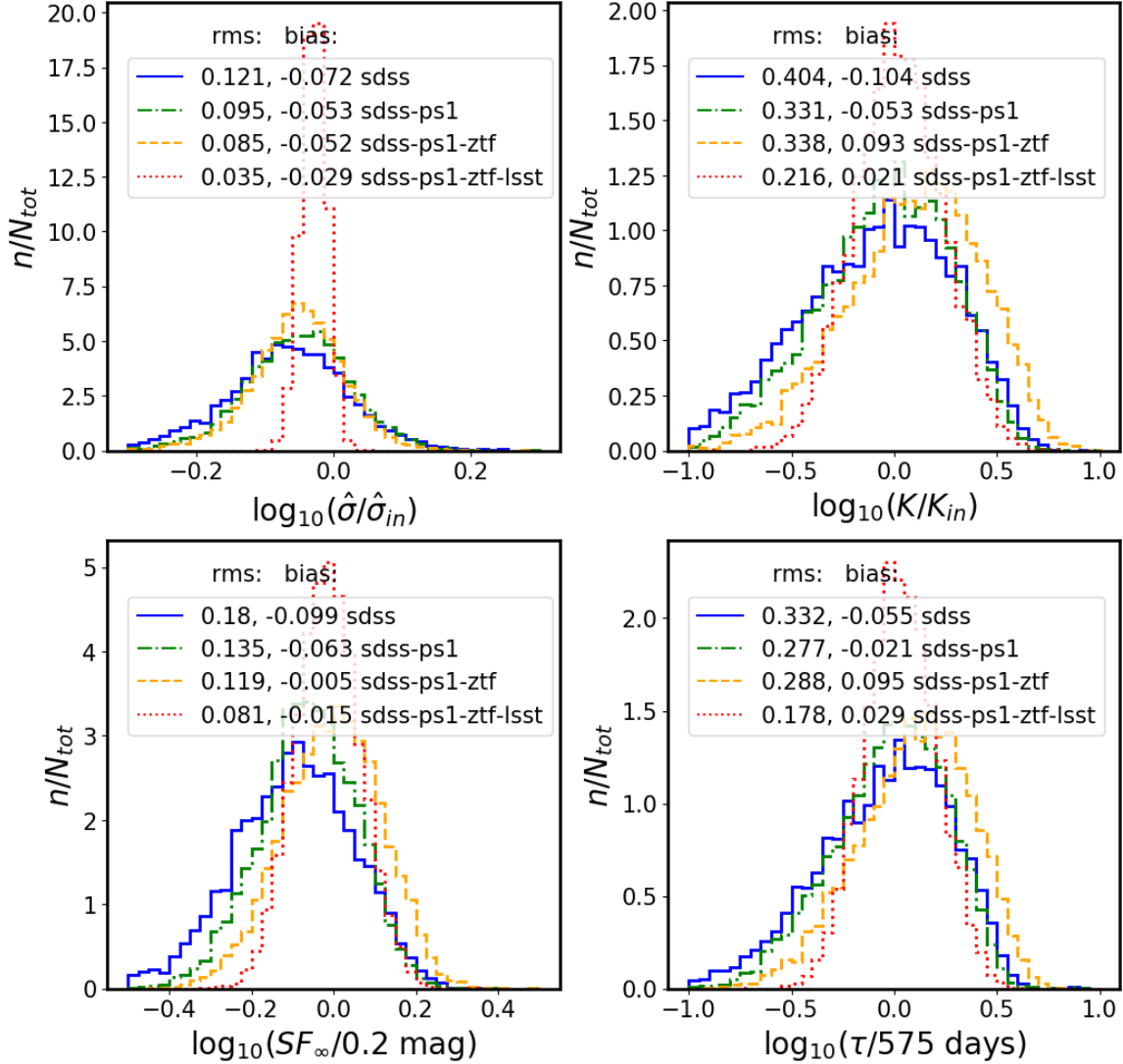
Figure 9. Comparison of retrieved parameters in relation to input parameters, shown as Fig.18 in MacLeod et al. (2011)

in this study we use the absolute i-band magnitude K-corrected to z=2: $M_i(z = 2)$.

These methods were used to create catalogs of quasar properties derived from spectra. Since quasars are variable at ∼0.2 mag level, the ideal is to use a single-epoch calibrated spectrum to estimate the continuum luminosity, and find virial black hole masses using relationships based on the monochromatic fluxes and broad line widths described above. A glance at the available quasar catalogs reveals that, given any SDSS data release, there is indeed first a catalog of basic quasar properties (redshift and photometry - eg. Schneider et al. 2007, 2010), and more detailed catalogs containing black hole masses and bolometric luminosities follow (eg. Shen et al. 2008, 2011). More recently, once SDSS DR12 Quasar Catalog (Pâris et al. 2017) was released, Kozłowski, Szymon 2017 followed using SDSS photometry as a proxy for monochromatic luminosities. Chen et al. (2018) added a detailed analysis of continuum luminosities in the Hα, Hβ regions for low-redshift quasars. Using the spectra from Chinese LAMOST survey Dong et al. (2018) also sought to estimate virial black hole masses, and the results, while consistent with Shen et al. (2011), suffered from the necessity to peg the non-calibrated spectra to the SDSS photometry which was taken a different epoch. Thus even though the SDSS DR12 Quasar Catalog of Pâris et al. (2018) is the most recent, like Pâris et al. (2017) it lacks black hole masses and bolometric luminosities, and there is no recent work that re-analyzed the spectral data. Therefore we use black hole mass estimates and monochromatic luminosities from Shen et al. (2011), based directly on single-epoch spectra.

5.4. *Trends in Quasar Properties*
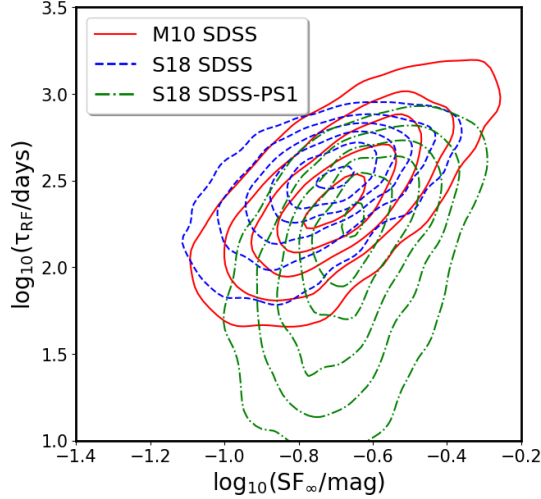
Figure 10. Comparison of distributions of the rest-frame variability timescale τ_{RF} against the asymptotic variability amplitude SF_∞, for M10 SDSS r-band, and celerite fits using SDSS or SDSS-PS1 segments of combined S82 quasar light curves. The M10 (red,solid lines) and this work, using only SDSS (dashed, blue), overlap, as we recover the same underlying distributions.
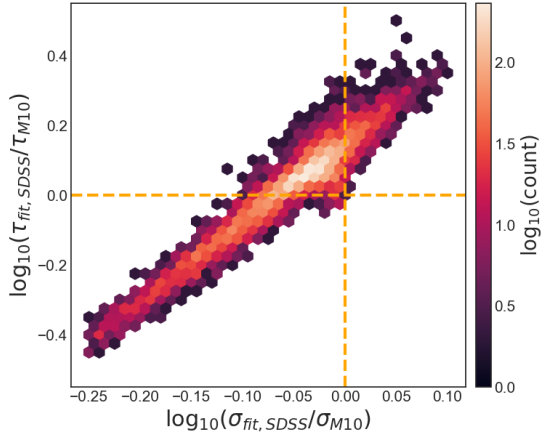
Figure 11. Comparison of celerite fits using only the SDSS r-band segments of S82 quasars $(\sigma_{fit}, \tau_{fit})$, against results of M10 for SDSS r-band $(\sigma_{M10}, \tau_{M10})$, object-by-object. The small offset can be attributed to software differences. See Fig. 10 for a comparison of rest-frame τ and SF_∞ distributions. This is similar to Fig.3 in M10, except we plot only the r-band SDSS results.

First, we consider quasar physical properties, which were updated between Shen et al. 2008 (M10) and Shen et al. 2011 (used here). Fig. 13 shows the distribution of quasars as a function of redshift z, absolute magnitude M_i, and black hole mass M_{BH}, and illustrates the fact that some trends are due to selection effects. For instance, the trend of increasing redshift with M_i on the upper left and bottom left panels, is partially due to the
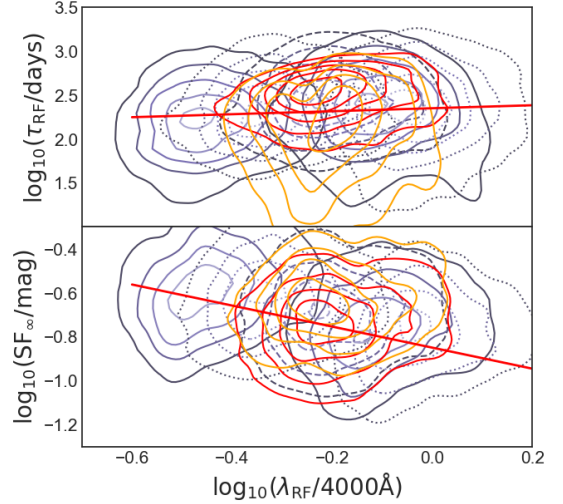
Figure 12. Rest-frame timescale τ (top panel), and asymptotic structure function SF_∞ (bottom panel), as a function of rest-frame wavelength λ_{RF}. The background contours show M10 SDSS *ugriz* data, and the foreground contours denote our results using SDSS (red) and SDSS-PS1 (orange) segments. The red line indicates the best-fit power law to M10 data, with $B = 0.17$ an -0.479 for τ_{RF}, and SF_∞, respectively.

fact that quasars have to be brighter to be included in the survey at increasing distances (luminosity-redshift degeneracy: see Sec.5, Fig.12 in M10, and Dong et al. 2018). Higher redshift quasars are also more active and have higher black hole masses due to cosmological downsizing (see Babić et al. 2007; Labita et al. 2009; McLure & Dunlop 2004).

5.5. *Trends with Luminosity, Black Hole Mass, and Redshift*

Fig. 14 shows τ and SF_∞ as a function of M_{BH}, M_i, and z. Correlations between variability parameters and the physical properties of quasars are of high utility. In the era of large synoptic surveys (ZTF, LSST), only a few percent of AGN with optical time-series will be followed up with spectroscopy (Ivezić et al. 2019). A relationship where $(\tau, SF_\infty) = f(M_i, M_{BH})$ would allow to infer black hole masses and luminosities for millions of quasars.

Some trends are dominant. For instance, brighter quasars have lower variability amplitude (upper-left panel), and this trend is largely independent of black hole mass (bottom-left panel).

We investigate these correlations in more detail by fitting to τ or SF_∞ (called f below) a power law, using a Bayesian linear regression method (Kelly 2007) that incorporates measurement uncertainties in all latent variables :
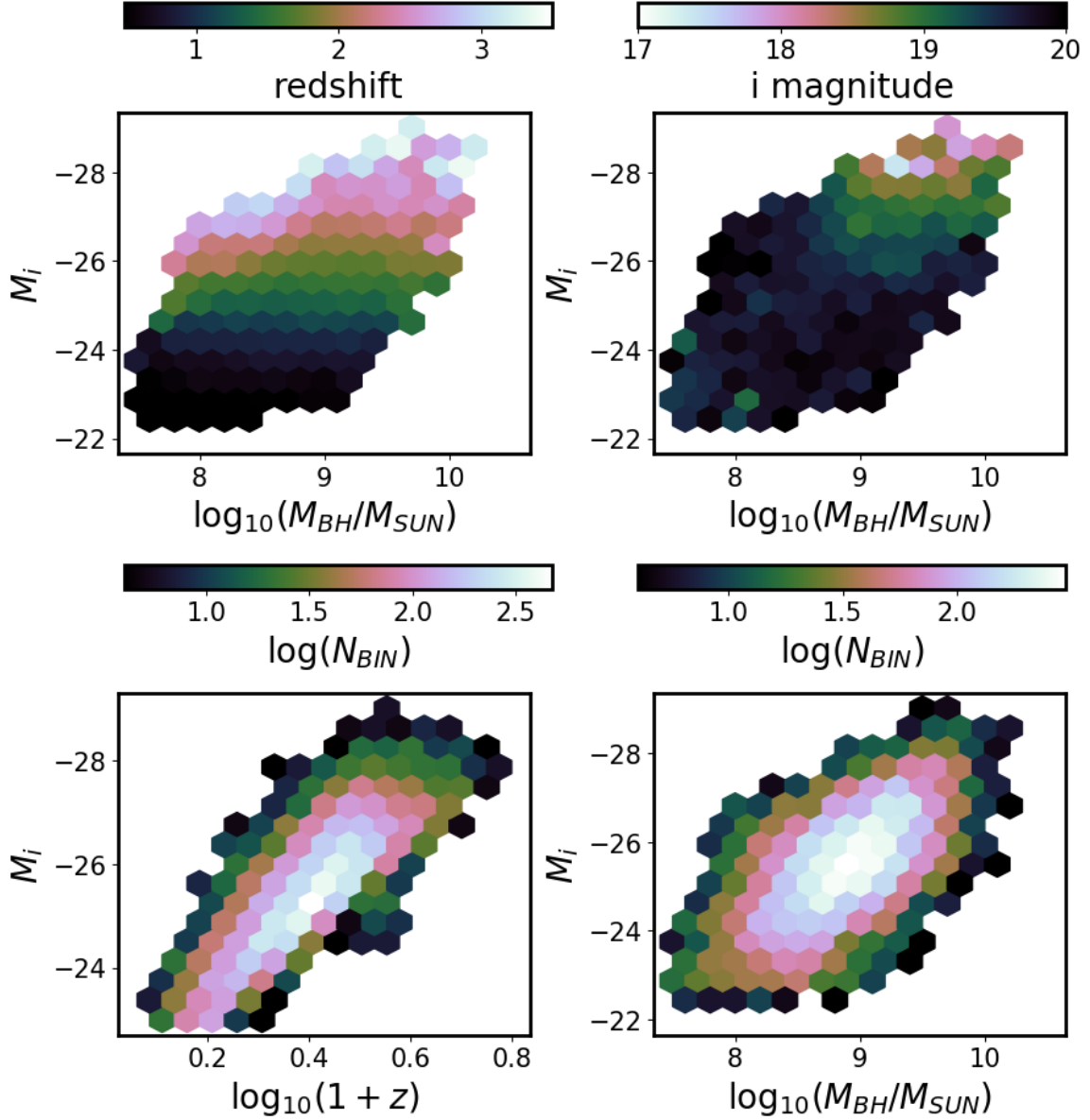
Figure 13. Distribution of quasars as a function of redshift, observed i-band magnitude, absolute i-band magnitude (K-corrected to z=2), and virial black hole mass. All quantities from (Shen et al. 2011).

$$\log_{10} f = A + B \log_{10} \left(\lambda_{RF}/4000\text{Å} \right) + C(M_i + 23)$$
$$+ D \log_{10} \left(M_{BH}/10^9 M_\odot \right) \qquad (13)$$

M10 fitted this model independently to each of the five SDSS bands, reporting the band-averaged coefficients - Fig. 15 shows the example of posterior samples for $f = SF_\infty$, illustrating that each band yields slightly different results.

Since we use combined SDSS-PS1 r-band data, we only compare our results to M10 SDSS r-band. Figs. 16 and 17 show the MCMC posterior draws from fitting Eq. 13 to M10, as well as our SDSS, SDSS-PS1 results

(S19, this work). Mean and standard deviation of each distribution are summarized in Table 2. For $f=\tau$ above, Fig. 16 shows that the new data supports a stronger dependence of variability amplitude on quasar luminosity by 0.04 dex ($C\sim0.06$ rather than ~0.02), but a smaller dependence on the black hole mass ($D\sim0.09$ rather than ~0.16). For $f=SF_\infty$ above, Fig. 17 shows that there is a weaker trend with both luminosity ($C\sim0.105$ rather than ~0.117) and black hole mass ($D\sim0.11$ rather than ~0.12), although the latter is a very small change.

5.6. Comparison to other studies: Eddington ratio
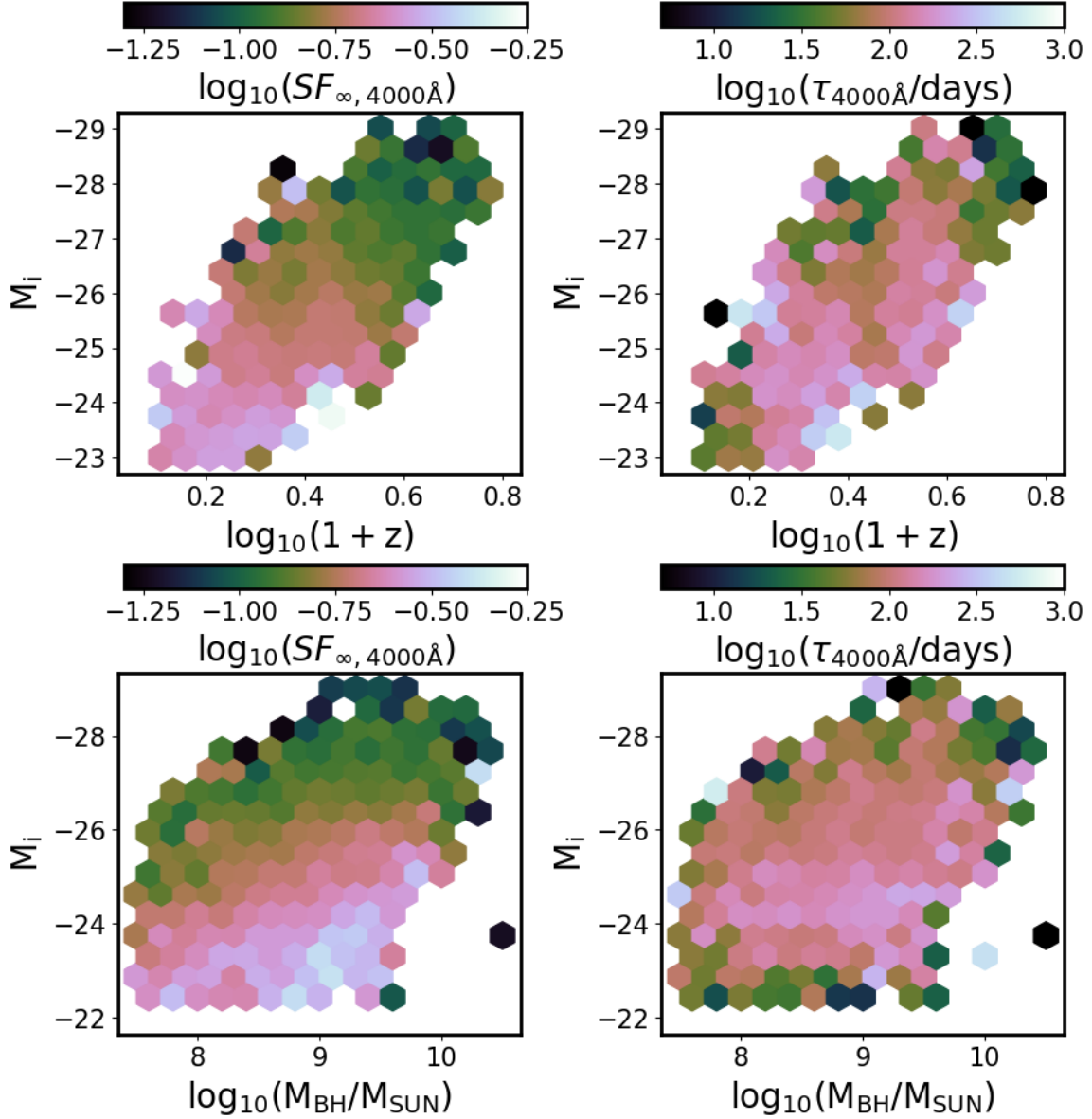
Figure 14. Long-term variability (SF_∞), and characteristic timescale (τ), as a function of absolute i-band magnitude (K-corrected to redshift 2, proxy for bolometric luminosity), virial black hole mass, and redshift.

Dependence of both τ and SF_∞ on black hole mass and quasar luminosity can be understood as a function of accretion rate, encoded in the Eddington ratio: $f_{Edd}=L_{Bol}/L_{Edd}$, where $L_{Edd}=1.26\times10^{38}(M_{BH}/M_\odot)$ erg/s (Shen et al. 2011). Fig.18 shows the dependence of f_{Edd} on M_i, M_{BH} and SF_∞, using SDSS-PS1 data. We find a much steeper power-law slope of -0.9, against -0.23 reported in M10 from SDSS data.

Additional PS1 data extending SDSS quasar light curves suggests that characteristic variability timescale is more strongly dependent on luminosity. This is consistent with Sun et al. (2018), who concluded with Structure Function analysis of their luminosity-matched

quasar sample, that τ depends mostly on the bolometric luminosity.

Anticorrelation of variability amplitude with the Eddington ratio has a variety of possible theoretical explanations. In the thin disk theory Shakura & Sunyaev (1973); Frank et al. (2002); Netzer (2013), radius of the emission region at given wavelength increases with the Eddington ratio, and is inversely proportional to temperatureRakshit & Stalin (2017). Thus a hotter disk means that the emission observed in a given bandpass is emitted from a larger radius. From causality, a smaller region can be more variable than a larger one. Therefore, a hotter disk would be less variable at a given wavelength
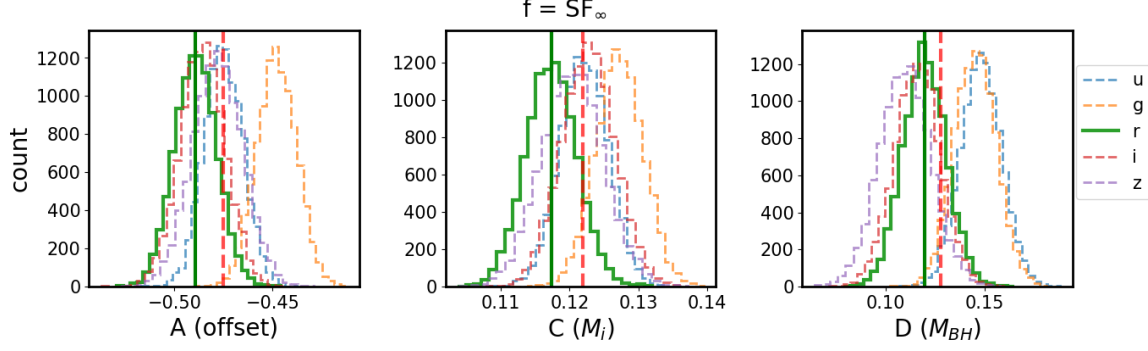
Figure 15. Table 1 in M10 reported the band-averaged values for fit coefficients A,C,D for Eq. 13. Shown here are samples from posterior MCMC draws using M10 results for $f = SF_\infty$, against Shen et al. 2011 M_i and M_{BH}. Because the mean of posterior for SDSS r-band results only (bold, solid lines) are different from the mean of band-averaged values (dashed lines), we compare our SDSS-PS1 combined r-band results against M10 SDSS r-band only.

Table 2. Comparison of best-fit coefficients for Eq. 13 using M10 results, and this work (S18). B is set to 0.17 or 0.479 from fitting a power law between λ_{RF} and τ, SF_∞ (see Fig. 12). For $f = \tau$, both C and D are almost the same between M10 and this work using SDSS only (rows 1 and 2). When using SDSS-PS1, C increases, and D is smaller than before (row 3). For $f = SF_\infty$, C and D are also the same between M10 and S19, SDSS (rows 4, 5), but when adding PS1 data, C and D become smaller (row 6).

f	Source	A(offset)	$B(\lambda_{RF})$	$C(M_i)$	$D(M_{\rm BH})$
τ	M10, SDSS	2.432 ± 0.026	0.17 ± 0.02	0.011 ± 0.009	0.163 ± 0.026
	S19, SDSS	2.603 ± 0.021	0.17 ± 0.02	0.022 ± 0.007	0.164 ± 0.021
	S19, SDSS-PS1	2.232 ± 0.029	0.17 ± 0.02	0.064 ± 0.01	0.094 ± 0.029
SF_∞	M10, SDSS	-0.489 ± 0.011	-0.479 ± 0.005	0.117 ± 0.004	0.12 ± 0.011
	S19, SDSS	-0.517 ± 0.01	-0.479 ± 0.005	0.117 ± 0.003	0.12 ± 0.01
	S19, SDSS-PS1	-0.467 ± 0.009	-0.479 ± 0.005	0.105 ± 0.003	0.111 ± 0.009
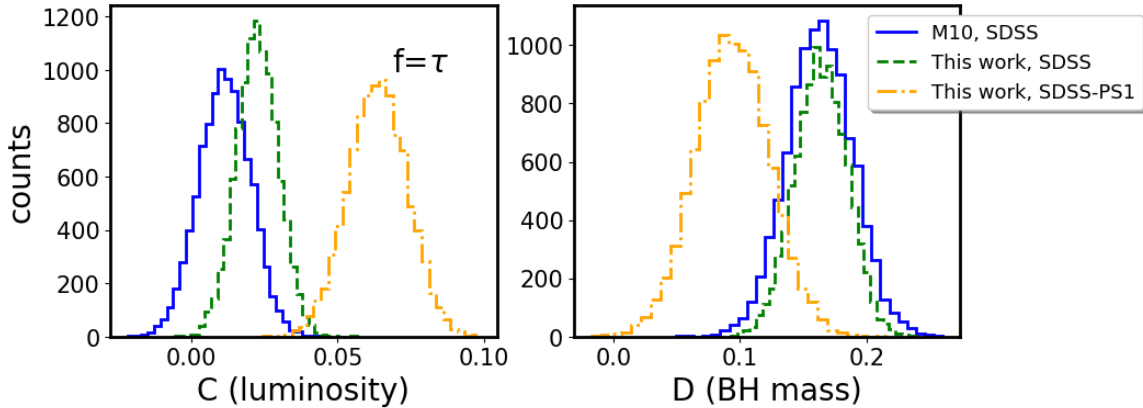
Figure 16. Distribution of posterior draws from MCMC Eq. 13, for $f = \tau$ with SDSS only (dashed green line), or SDSS-PS1 (dot-dashed yellow line) combined quasar light curves, against M10 SDSS r-band. The results from SDSS-only portion are consistent with M10 for the single band. Inclusion of the PS1 portion decreases the timescale dependence on black hole mass, but increases the luminosity dependence. This can be understood as a rotation of the plane in (τ, M_i, M_{BH}) coordinates.
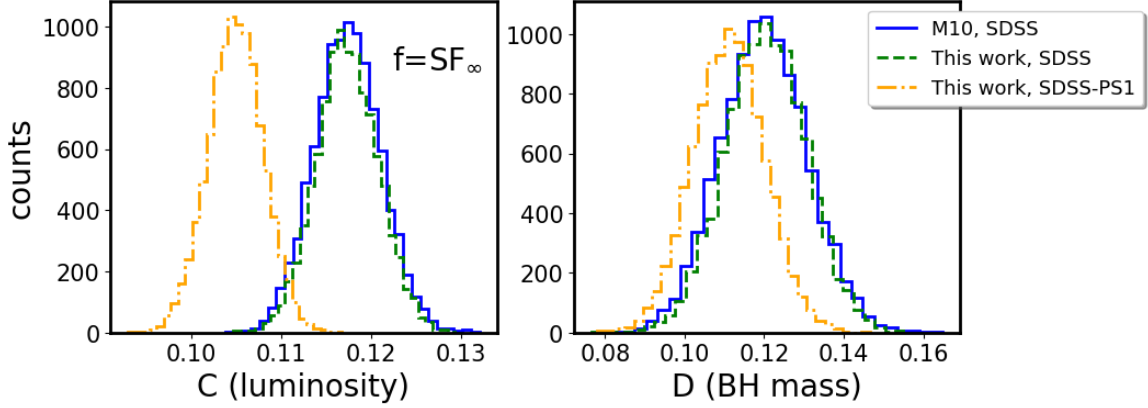
Figure 17. Same as Fig. 16, but fitting quasar absolute magnitude, and black hole mass in Eq. 13 as a function of the asymptotic amplitude $f = SF_\infty$. New data from PS1 supports a weaker dependence of variability amplitude with luminosity and black hole mass.
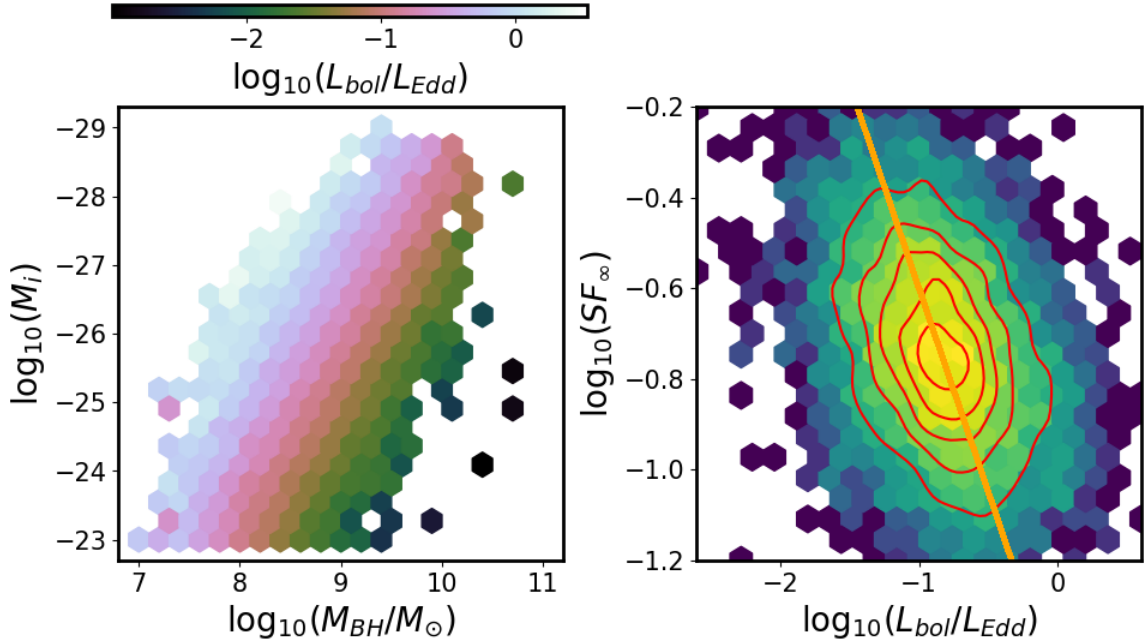
Figure 18. Left : the Eddigton ratio L/L_{Edd} (from Shen et al. 2011) plotted as a function of M_{BH} vs M_i. Right: the asymptotic variability amplitude SF_∞, corrected for the wavelength dependence to 4000Å, as a function of the Eddington ratio. The slope of -0.9 (solid line) is much steeper than -0.23 found by M10 with the SDSS only data.

than a colder one, and the variability amplitude as studied in a particular bandpass (here, SDSS r-band) would be anticorrelated with Eddington ratio (Fausnaugh et al. 2016; Edelson et al. 2015).

On the other hand, in the strongly inhomogeneous disk model Dexter & Agol (2011) independent temperature fluctuations in N zones drive the variability. In that framework the inverse trend of variability amplitude against L/L_{Edd} and L_{Bol} can be understood qualitatively if more luminous quasars also have higher mass accretion rate, and thus greater number of disk inhomogeneities, resulting in smaller flux variability (Simm et al. 2016). The inhomogeneous disk model was consistent with mean SDSS spectral analysis in Ruan et al. (2014), but was not a preferreed explanation for Kokubo (2015).

Both Rumbaugh et al. 2018 (with Dark Energy Survey structure function study) and Sun et al. (2018) (with a low-z subsample of S82 SDSS quasars) confirm the anti-correlation between quasar variability and luminosity. However, Graham et al. 2019 do not find support for this trend with the sample extremely variable quasars (EVQs) in the CRTS dataset, but when selecting for lower luminosity sources ($M_V < -23$), the anti-correlation is recovered. This is in accord with an interpretation that a dwindling fuel supply may correspond to higher variability. Furthemore, Sánchez-Sáez et al. (2018) combined the SDSS spectra with 5 year light curves of 2345 quasars obtained with Quasar Equatorial Survey Team (QUEST)-La Silla AGN Variability Survey, and using the Bayesian parametrization of Structure Function (Schmidt et al. 2010), $\mathrm{SF}(\tau) = A(\tau/1\mathrm{yr})^\gamma$, they also found that the amplitude of variability A is anti-correlated with rest-frame emission wavelength, and Eddington ratio (also see Simm et al. 2016, Rakshit & Stalin 2017).

Indeed, f_{Edd} is a proxy for the strength of accretion, which together with orientation may be the key to explaining quasar main sequence (QMS) (Shen & Ho 2014; Marziani et al. 2018). The QMS, defined by so-called Eigenvector-1, is the the anti-correlation between the broad line FeII emission, and the strength of the narrow OIII (5007Å) line (Wang et al. 1996). An analysis of quasar clustering (Shen & Ho 2014), later confirmed by Sun & Shen (2015) with measurements of black hole mass from the quasar host galaxy stellar dispersion (Ferrarese & Merritt 2000; Kormendy & Ho 2013), showed that the entire diversity of quasars in QMS can be explained by the variation in accretion (affecting R_{FeII} - the ratio of the FeII EQ between $4435 - 4685$ Å and $\mathrm{H}\beta$), or orientation effects (affecting the FWHM of the $\mathrm{H}\beta$). However, Panda et al. (2019a,b) found that these

are insufficient, and variations in metallicity, as well as a range of cloud densities, and turbulences are required. Jiang et al. (2016) also found that metallicity, and in particular the iron opacity bump, may have a strong influence on the stability of an accretion disk, and thus linking metallicity to AGN variability. This is also consistent with findings of Sun et al. (2018): quasars with high FeII strength have higher metallicity, and have more stable disks.

5.7. *Variability Timescales*

In the era of changing-look active galaxies (including initially distinct classes of Changing-Look Quasars (LaMassa et al. 2015; MacLeod et al. 2019), Changing-Look AGNs (Marchese et al. 2012; Bianchi et al. 2009; Risaliti et al. 2009), Changing-Look LINERS (Frederick et al. 2019) to name a few) there is a revived interest in possibly linking the behavior of stellar-sized accreting systems (eg. Black Hole Binaries), to that of galactic scale (eg. AGN, QSO, LINERS)(Noda & Done 2018; Ruan et al. 2019).

It appears that there are several timescales at play, and possibly several interlinked mechanisms that drive the variability.

There is a hierarchy of relevant timescales in the standard optically thick, geometrically thin, α-disk model : dynamical, thermal, front, viscous, with $t_{dyn} < t_{th} < t_{front} < t_{visc}$ (Netzer 2013; Frank et al. 2002).

The dynamical, or gas orbital, timescale is simply an inverse of the Keplerian orbital angular frequency Ω at radius R :

$$t_{dyn} \sim 1/\Omega = \left(\frac{GM}{R^3}\right)^{-1/2} \tag{14}$$

The main parameter describing the accretion disk is α - the ratio of the (vertically averaged) total stress to thermal (vertically averaged) pressure (Lasota 2016) :

$$\alpha = \frac{\langle \tau_{r\varphi}\rangle_z}{\langle P\rangle_z} \tag{15}$$

After Lasota (2016), the hydrodynamical stress tensor (corresponding to kinematic viscocity ν) is:

$$\tau_{r\varphi} = \rho\nu\frac{\partial v_\varphi}{\partial R} = \rho\nu\frac{d\Omega}{d\ln R} = \frac{3\rho\nu\Omega}{2} \tag{16}$$

so with c_s - local sound speed at radius R (isothermal sound speed is $c_s = \sqrt{P/\rho}$),

$$\alpha = \frac{3\rho\nu\Omega}{2P} = \frac{3\Omega\nu}{2c_s^2} \tag{17}$$

This means that smaller α corresponds to less viscous disks.

The thermal timescale, related to the time needed for re-adjustment to the thermal equilibrium (derived in detail in Frank et al. (2002)), is the ratio of heat content per unit disk area to dissipation rate per unit disk area: $(dE/A)/(dE/dt/A) = dt$. The heat content per unit volume is $\sim \rho kT/\mu m_p \sim \rho c_s^2$, and heat content per unit area is $\sim \rho c_s^2/h \sim \Sigma c_s^2$. Meanwhile, the dissipation rate per unit area, $D(R)$, is

$$D(R) = \frac{9}{8}\nu \Sigma R^{-3} GM \qquad (18)$$

(eq. 4.30 in Frank et al. 2002), so :

$$t_{th} \sim \frac{c_s^2 R^3}{GM\nu} = \frac{c_s^2}{\nu \Omega} = \frac{t_{dyn}}{\alpha} \qquad (19)$$

Thus if the disk were inviscid ($\nu \to 0$), then $t_{th} \to \infty$ i.e. there is no contact with adjacent disk elements.

The cooling and heating fronts propagate through the disk at αc_s (Hameury et al. 2009) - in that description with no viscosity there is no communication between neighboring disk annuli, and thus no front propagation (Balbus & Hawley 1998; Balbus 2003). Following Stern et al. (2018), if we define as h/R the the disk aspect ratio, with the disk height $h = c_s/\Omega$, the characteristic time for front propagation is:

$$t_{front} \sim (h/R)^{-1} t_{th} \qquad (20)$$

The viscous timescale is the characteristic time it would take for a parcel of material to undergo a radial transport due to the viscous torques from the radius R to the black hole (Czerny 2006). Note that while viscosity has probably magnetic origin (Eardley & Lightman 1975; Grzędzielski et al. 2017), in this simplistic order of magnitude estimate we use a hydrodynamical description of accretion flow. With $\nu = \eta/\rho$ (kinematic viscosity being the ratio of dynamical viscosity to density), Frank et al. (2002) shows (Chap.5.2) that

$$t_{visc} \sim R^2/\nu \sim R/v_R = (h/R)^{-2} t_{th} \qquad (21)$$

We can parametrize each timescale for a black hole mass $M_{BH} = 10^8 M_\odot$, at $R \sim 150 r_g$, with the gravitational radius $r_g = GM_{BH}/c^2 \sim 4au$, using Eqs.5-8 in Stern et al. (2018) :

$$t_{dyn} \sim 10 \text{days} \left(\frac{M_{BH}}{10^8 M_\odot}\right) \left(\frac{R}{150 r_g}\right)^{3/2} \qquad (22)$$

$$t_{th} \sim 1 \text{ year} \left(\frac{\alpha}{0.03}\right)^{-1} \left(\frac{M_{BH}}{10^8 M_\odot}\right) \left(\frac{R}{150 r_g}\right)^{3/2} \qquad (23)$$

$$t_{front} \sim 20 \text{ years} \left(\frac{h/R}{0.05}\right)^{-1} \left(\frac{\alpha}{0.03}\right)^{-1} \left(\frac{M_{BH}}{10^8 M_\odot}\right) \left(\frac{R}{150 r_g}\right)^{3/2} \qquad (24)$$

$$t_{visc} \sim 400 \text{ years} \left(\frac{h/R}{0.05}\right)^{-2} \left(\frac{\alpha}{0.03}\right)^{-1} \left(\frac{M_{BH}}{10^8 M_\odot}\right) \left(\frac{R}{150 r_g}\right)^{3/2} \qquad (25)$$

In summary, of considered timescales only thermal and dynamical are short enough to be related to the observed short-term stochastic variability. It may be that the variability on the scale of days is driven by local changes, and on the longer scale (perhaps hundreds of days) by a different mechanism (Kokubo 2015). The other time scales may be more related to the dramatic changes in brightness of the continuum as observed in changing-look AGN - Noda & Done (2018) favor a change in mass accretion rate, followed by a propagation of the cooling front Lawrence (2018); Simm et al. (2016). Noda & Done (2018) also suggests that perhaps short-term variability could be related to the amount of the disk swept by the thermal front propagation due to Hydrogen ionization instability, similarly to white dwarf systems (also, see Ruan et al. 2019; Ross et al. 2018; Śniegowska & Czerny 2019).

The variability on several years timescale could also be explained by the X-ray reprocessing model Kokubo (2015); Kubota & Done (2018), assuming that the AGN UV-optical variability is a results of reprocessing of X-ray or far-UV emission (Krolik et al. 1991). The idea of X-ray reprocessing over time has gained more and more support, with evidence from simultaneous X-ray-UV-optical AGN time series (Edelson et al. 2014; McHardy et al. 2018; Zhu et al. 2018). In particular, the accretion disk blackbody emission is insufficient to explain the broadband AGN spectrum. The total SED with a soft X-ray excess, and a hard X-ray tail, requires additional sources of emission (Kubota & Done 2018). A novel model by Kubota & Done (2018) divides the flow into blackbody emission, warm Comptonization region (the disk), and hard X-ray hot Comptonization component (corona, or a hot material filling the region close to the black hole below the truncation radius). Since the soft X-rays are correlated with the hard X-rays, at least part of the picture consists of reflection or reprocessing of hard X-rays by the disk (Lawrence 2018). This model predicts an increase of variability amplitude (SF_∞) with

M_{BH}, and adds an insight that the observed slope is due to changes in accretion rate $\dot{m}$, explaining that smaller $\dot{m}$ corresponds to highest variability. This qualitatively agrees with the picture that dwindling fuel supply makes the flow more variable. Previous worries about X-ray reprocessing concerned the seemingly insufficient solid angle subtended by the source of the hard X-rays to cause the observed soft X-ray and optical response. This is addressed by realizing that reprocessing could be taking place in the extended region (**?**), such as an inflated inner disk (corresponding to warm Comptonizing region in Kubota & Done (2018)), or even the BLR region serving as an additional 'complex reprocessor'(McHardy et al. 2018). Also, for Panda et al. (2019a) warm corona helps decrease the dependence of $R_{\rm FeII}$ on f_{Edd}.

Thus while CLAGN may be related to the state-change to ADAF flow (Śniegowska & Czerny 2019) similar to that of XRBs (Noda & Done 2018; Ruan et al. 2019), with cooling and heating fronts (**?**), the more short-timescale variability requires approximately three distinct emission regions (Kubota & Done 2018), with extended reprocessor (diffuse, hot, puffed-up inner disk, and BLR - McHardy et al. 2018), that reverberates the rapid hard X-ray variability in soft X-rays to optical via UV (**?**). Some emission (especially soft X-rays) seems to require the warm Comptonizing corona Kubota & Done (2018). The warm corona, coupled with metallicity changes, and variation in turbulence level and cloud density, also helps explain the Quasar Main Sequence in the optical (Panda et al. 2019a,b). Finally, the Kubota & Done (2018) model, apart from being consistent with other mechanisms (McHardy et al. 2018; Panda et al. 2019a; Śniegowska & Czerny 2019; Lawrence 2018; Ross et al. 2018; Ruan et al. 2019), explains the observed correlation of variability amplitude with black hole mass as corresponding to variations in mass accretion rate.

6. CONCLUSIONS

We modeled $\sim$9000 Stripe82 quasars by the Damped Random Walk (DRW) model using Gaussian Processes implemented in celerite. We show that by extending the SDSS Stripe82 light curves with PS1 data we can improve on the recovery of the DRW parameters: characteristic timescale τ and asymptotic variability amplitude SF_∞. We find that these correlate with black hole mass M_{BH} and absolute i-band magnitude M_i, with τ more dependent on M_i and less on M_{BH} than in M10. SF_∞ is less strongly driven by M_i and M_{BH} than M10 found, and has a stronger, almost inverse, dependence on the Eddington ratio f_{Edd}. This is consistent with lower mass accretion rate corresponding to higher variability, so that when the supply of fuel decreases, the

flow becomes less stable, more clumpy, more inhomogeneous, radiate at larger distances. This is also consistent with the X-ray reprocessing model, whereby the hard X-ray variability of the inner disk is reflected/reprocessed by the extended warm Comptonization region (inflated disk), and perhaps a complex reprocessor, including the clouds of the broad line region. Changes on recovered timescales are too fast to be driven by changes in disk viscosity, or thermal front propagation alone - thermal or dynamical timescale of response to the X-ray emission seems most consistent with our results.

More data extending the light curves would help improve the fit coefficients, decreasing the scatter in observed correlations. Better measurements of quasar properties would be also of high utility - the uncertainty in black hole mass is one of the biggest sources of error. This will be possible by extensions to existing AGN reverberation mapping campaigns (SDSS-IV RM), providing better calibration for line width-based methods of estimating black hole masses. All quasars in this study were spectroscopically confirmed, but some spectra had low signal-to-noise, resulting in higher likelihood of incorrect redshift measurement. Better spectroscopy and follow up of S82 quasars would not only help improve on the spectrum-based properties (redshift, absolute magnitude, black hole masses), but also allow to study spectral changes, and possibly new CLQSO discoveries.

If this study were to be expanded onto a sample of quasars with good photometry over sufficiently long baselines, but lacking spectral information, the required physical information on quasars could be obtained by indirect methods of estimating the coarse spectral information from broad-band photometry. This would benefit from better catalogs of existing spectroscopically-confirmed quasars to improve the calibration, as well as better methods of estimating the redshift based on photometry alone (photo-z).

This will be possible in short term with the ZTF, and in the long term with LSST. Occasional coverage adding few epochs to some quasars may be possible with other surveys (eg. TESS), but to improve the statistics an entire sample of S82 quasars would require longer baselines.

7. ACKNOWLEDGEMENTS

REFERENCES

AlSayyad, Y. 2016, PhD thesis, University of Washington. http://hdl.handle.net/1773/37020

Ambikasaran, S., Foreman-Mackey, D., Greengard, L., Hogg, D. W., & O'Neil, M. 2015, IEEE Transactions on Pattern Analysis and Machine Intelligence, 38, doi: 10.1109/TPAMI.2015.2448083

Annis, J., Soares-Santos, M., Strauss, M. A., et al. 2014, ApJ, 794, 120, doi: 10.1088/0004-637X/794/2/120

Aranzana, E., Körding, E., Uttley, P., Scaringi, S., & Bloemen, S. 2018, MNRAS, 476, 2501, doi: 10.1093/mnras/sty413

Babić, A., Miller, L., Jarvis, M. J., et al. 2007, A&A, 474, 755, doi: 10.1051/0004-6361:20078286

Balbus, S. A. 2003, ARA&A, 41, 555, doi: 10.1146/annurev.astro.41.081401.155207

Balbus, S. A., & Hawley, J. F. 1998, Reviews of Modern Physics, 70, 1, doi: 10.1103/RevModPhys.70.1

Bauer, A., Baltay, C., Coppi, P., et al. 2009, ApJ, 696, 1241, doi: 10.1088/0004-637X/696/2/1241

Bentz, M. C., Peterson, B. M., Netzer, H., Pogge, R. W., & Vestergaard, M. 2009, ApJ, 697, 160, doi: 10.1088/0004-637X/697/1/160

Bianchi, S., Piconcelli, E., Chiaberge, M., et al. 2009, ApJ, 695, 781, doi: 10.1088/0004-637X/695/1/781

Blanton, M. R., Lin, H., Lupton, R. H., et al. 2003, AJ, 125, 2276, doi: 10.1086/344761

Borucki, W. J., Koch, D., Basri, G., et al. 2010, Science, 327, 977, doi: 10.1126/science.1185402

Cai, Z.-Y., Wang, J.-X., Gu, W.-M., et al. 2016, ApJ, 826, 7, doi: 10.3847/0004-637X/826/1/7

Caplar, N., Lilly, S. J., & Trakhtenbrot, B. 2017, ApJ, 834, 111, doi: 10.3847/1538-4357/834/2/111

Chambers, K. C. 2011, in Bulletin of the American Astronomical Society, Vol. 43, American Astronomical Society Meeting Abstracts #218, 113.01

Chen, Z.-F., Pan, D.-S., Pang, T.-T., & Huang, Y. 2018, ApJS, 234, 16, doi: 10.3847/1538-4365/aa9d90

Czerny, B. 2006, in Astronomical Society of the Pacific Conference Series, Vol. 360, AGN Variability from X-Rays to Radio Waves, ed. C. M. Gaskell, I. M. McHardy, B. M. Peterson, & S. G. Sergeev, 265

Dexter, J., & Agol, E. 2011, ApJL, 727, L24, doi: 10.1088/2041-8205/727/1/L24

Dexter, J., & Begelman, M. C. 2019, MNRAS, 483, L17, doi: 10.1093/mnrasl/sly213

Dong, X. Y., Wu, X.-B., Ai, Y. L., et al. 2018, AJ, 155, 189, doi: 10.3847/1538-3881/aab5ae

Drake, A. J., Djorgovski, S. G., Mahabal, A., et al. 2009, ApJ, 696, 870, doi: 10.1088/0004-637X/696/1/870

Eardley, D. M., & Lightman, A. P. 1975, ApJ, 200, 187, doi: 10.1086/153777

Edelson, R., Vaughan, S., Malkan, M., et al. 2014, ApJ, 795, 2, doi: 10.1088/0004-637X/795/1/2

Edelson, R., Gelbord, J. M., Horne, K., et al. 2015, ApJ, 806, 129, doi: 10.1088/0004-637X/806/1/129

Edelson, R., Gelbord, J., Cackett, E., et al. 2019, ApJ, 870, 123, doi: 10.3847/1538-4357/aaf3b4

Fausnaugh, M. M., Denney, K. D., Barth, A. J., et al. 2016, ApJ, 821, 56, doi: 10.3847/0004-637X/821/1/56

Ferrarese, L., & Merritt, D. 2000, The Astrophysical Journal, 539, L9, doi: 10.1086/312838

Flewelling, H. 2018, in American Astronomical Society Meeting Abstracts, Vol. 231, American Astronomical Society Meeting Abstracts 231, 436.01

Foreman-Mackey, D., Agol, E., Angus, R., & Ambikasaran, S. 2017, ArXiv e-prints. https://arxiv.org/abs/1703.09710

Foreman-Mackey, D., Bernhard, J., Hoyer, S., Walker, S., & Angus, R. 2018, dfm/george: george v0.3.1, doi: 10.5281/zenodo.1137793. https://doi.org/10.5281/zenodo.1137793

Frank, J., King, A., & Raine, D. J. 2002, Accretion Power in Astrophysics: Third Edition (Cambridge University Press), 398

Frederick, S., Gezari, S., Graham, M. J., et al. 2019, arXiv e-prints, arXiv:1904.10973. https://arxiv.org/abs/1904.10973

Gaskell, C. M., & Peterson, B. M. 1987, ApJS, 65, 1, doi: 10.1086/191216

Graham, M. J., Djorgovski, S. G., Stern, D., et al. 2015, Nature, 518, 74, doi: 10.1038/nature14143

Graham, M. J., Ross, N. P., Stern, D., et al. 2019, arXiv e-prints, arXiv:1905.02262. https://arxiv.org/abs/1905.02262

Grzędzielski, M., Janiuk, A., Czerny, B., & Wu, Q. 2017, A&A, 603, A110, doi: 10.1051/0004-6361/201629672

Guo, H., Wang, J., Cai, Z., & Sun, M. 2017, ApJ, 847, 132, doi: 10.3847/1538-4357/aa8d71

Hameury, J.-M., Viallet, M., & Lasota, J.-P. 2009, A&A, 496, 413, doi: 10.1051/0004-6361/200810928

Hernitschek, N., Schlafly, E. F., Sesar, B., et al. 2016, The Astrophysical Journal, 817, 73

Ivezić, Ž., Smith, J. A., Miknaitis, G., et al. 2007, AJ, 134, 973, doi: 10.1086/519976

Ivezić, Ž., Kahn, S. M., Tyson, J. A., et al. 2019, ApJ, 873, 111, doi: 10.3847/1538-4357/ab042c

Jiang, Y.-F., Davis, S. W., & Stone, J. M. 2016, ApJ, 827, 10, doi: 10.3847/0004-637X/827/1/10

Kasliwal, V. P., Vogeley, M. S., & Richards, G. T. 2015, MNRAS, 451, 4328, doi: 10.1093/mnras/stv1230

—. 2017, MNRAS, 470, 3027, doi: 10.1093/mnras/stx1420

Kelly, B. C. 2007, ApJ, 665, 1489, doi: 10.1086/519947

Kelly, B. C., Bechtold, J., & Siemiginowska, A. 2009, The Astrophysical Journal, 698, 895

Kelly, B. C., Becker, A. C., Sobolewska, M., Siemiginowska, A., & Uttley, P. 2014, ApJ, 788, 33, doi: 10.1088/0004-637X/788/1/33

Kelly, B. C., Treu, T., Malkan, M., Pancoast, A., & Woo, J.-H. 2013, ApJ, 779, 187, doi: 10.1088/0004-637X/779/2/187

Kokubo, M. 2015, MNRAS, 449, 94, doi: 10.1093/mnras/stv241

Kormendy, J., & Ho, L. C. 2013, ARA&A, 51, 511, doi: 10.1146/annurev-astro-082708-101811

Kozłowski, S. 2015, AcA, 65, 251. https://arxiv.org/abs/1504.05960

—. 2016, ApJ, 826, 118, doi: 10.3847/0004-637X/826/2/118

Kozłowski, S. 2016, MNRAS, 459, 2787, doi: 10.1093/mnras/stw819

Kozłowski, S. 2017, ApJS, 228, 9, doi: 10.3847/1538-4365/228/1/9

Kozłowski, S., Kochanek, C. S., Udalski, A., et al. 2010, ApJ, 708, 927

Kozłowski, Szymon. 2017, A&A, 597, A128, doi: 10.1051/0004-6361/201629890

Krolik, J. H., Horne, K., Kallman, T. R., et al. 1991, ApJ, 371, 541, doi: 10.1086/169918

Kubota, A., & Done, C. 2018, MNRAS, 480, 1247, doi: 10.1093/mnras/sty1890

Labita, M., Decarli, R., Treves, A., & Falomo, R. 2009, MNRAS, 399, 2099, doi: 10.1111/j.1365-2966.2009.15400.x

LaMassa, S. M., Cales, S., Moran, E. C., et al. 2015, ApJ, 800, 144, doi: 10.1088/0004-637X/800/2/144

Lasota, J.-P. 2016, in Astrophysics and Space Science Library, Vol. 440, Astrophysics of Black Holes: From Fundamental Aspects to Latest Developments, ed. C. Bambi, 1

Lawrence, A. 2018, Nature Astronomy, 2, 102, doi: 10.1038/s41550-017-0372-1

Li, Z., McGreer, I. D., Wu, X.-B., Fan, X., & Yang, Q. 2018, ApJ, 861, 6, doi: 10.3847/1538-4357/aac6ce

Lira, P., Arévalo, P., Uttley, P., McHardy, I. M. M., & Videla, L. 2015, MNRAS, 454, 368, doi: 10.1093/mnras/stv1945

MacLeod, C. L., Ivezić, Ž., Kochanek, C. S., et al. 2010, The Astrophysical Journal, 721, 1014

MacLeod, C. L., Brooks, K., Ivezić, Ž., et al. 2011, The Astrophysical Journal, 728, 26

MacLeod, C. L., Ivezić, Ž., Sesar, B., et al. 2012, The Astrophysical Journal, 753, 106

MacLeod, C. L., Green, P. J., Anderson, S. F., et al. 2019, ApJ, 874, 8, doi: 10.3847/1538-4357/ab05e2

Marchese, E., Braito, V., Della Ceca, R., Caccianiga, A., & Severgnini, P. 2012, Monthly Notices of the Royal Astronomical Society, 421, 1803, doi: 10.1111/j.1365-2966.2012.20445.x

Marziani, P., Dultzin, D., Sulentic, J. W., et al. 2018, Frontiers in Astronomy and Space Sciences, 5, 6, doi: 10.3389/fspas.2018.00006

McGreer, I. D., Fan, X., Jiang, L., & Cai, Z. 2018, AJ, 155, 131, doi: 10.3847/1538-3881/aaaab4

McGreer, I. D., Jiang, L., Fan, X., et al. 2013, ApJ, 768, 105, doi: 10.1088/0004-637X/768/2/105

McHardy, I. M., Connolly, S. D., Horne, K., et al. 2018, MNRAS, 480, 2881, doi: 10.1093/mnras/sty1983

McLure, R. J., & Dunlop, J. S. 2004, MNRAS, 352, 1390, doi: 10.1111/j.1365-2966.2004.08034.x

Mushotzky, R. F., Edelson, R., Baumgartner, W., & Gandhi, P. 2011, The Astrophysical Journal, 743, L12, doi: 10.1088/2041-8205/743/1/l12

Netzer, H. 2013, The Physics and Evolution of Active Galactic Nuclei (Cambridge University Press)

Noda, H., & Done, C. 2018, MNRAS, 480, 3898, doi: 10.1093/mnras/sty2032

Oke, J. B., & Sandage, A. 1968, ApJ, 154, 21, doi: 10.1086/149737

Palanque-Delabrouille, N., Magneville, C., Yèche, C., et al. 2013, A&A, 551, A29, doi: 10.1051/0004-6361/201220379

Panda, S., Czerny, B., Done, C., & Kubota, A. 2019a, ApJ, 875, 133, doi: 10.3847/1538-4357/ab11cb

Panda, S., Marziani, P., & Czerny, B. 2019b, arXiv e-prints, arXiv:1905.01729. https://arxiv.org/abs/1905.01729

Pâris, I., Petitjean, P., Ross, N. P., et al. 2017, A&A, 597, A79, doi: 10.1051/0004-6361/201527999

Pâris, I., Petitjean, P., Aubourg, É., et al. 2018, A&A, 613, A51, doi: 10.1051/0004-6361/201732445

Peterson, B. M., Ferrarese, L., Gilbert, K. M., et al. 2004, ApJ, 613, 682, doi: 10.1086/423269

Rakshit, S., & Stalin, C. S. 2017, ApJ, 842, 96, doi: 10.3847/1538-4357/aa72f4

Rau, A., Kulkarni, S. R., Law, N. M., et al. 2009, PASP, 121, 1334, doi: 10.1086/605911

Richards, G. T., Strauss, M. A., Fan, X., et al. 2006, AJ, 131, 2766, doi: 10.1086/503559

Risaliti, G., Miniutti, G., Elvis, M., et al. 2009, The Astrophysical Journal, 696, 160, doi: 10.1088/0004-637x/696/1/160

Ross, N. P., McGreer, I. D., White, M., et al. 2013, ApJ, 773, doi: 10.1088/0004-637X/773/1/14

Ross, N. P., Ford, K. E. S., Graham, M., et al. 2018, MNRAS, 480, 4468, doi: 10.1093/mnras/sty2002

Ruan, J. J., Anderson, S. F., Dexter, J., & Agol, E. 2014, The Astrophysical Journal, 783, 105, doi: 10.1088/0004-637x/783/2/105

Ruan, J. J., Anderson, S. F., Eracleous, M., et al. 2019, arXiv e-prints, arXiv:1903.02553. https://arxiv.org/abs/1903.02553

Rumbaugh, N., Shen, Y., Morganson, E., et al. 2018, ApJ, 854, 160, doi: 10.3847/1538-4357/aaa9b6

Rybicki, G. B., & Press, W. H. 1992, ApJ, 398, 169, doi: 10.1086/171845

Sánchez-Sáez, P., Lira, P., Mejía-Restrepo, J., et al. 2018, ApJ, 864, 87, doi: 10.3847/1538-4357/aad7f9

Schmidt, K. B., Marshall, P. J., Rix, H.-W., et al. 2010, ApJ, 714, 1194, doi: 10.1088/0004-637X/714/2/1194

Schneider, D. P., Hall, P. B., Richards, G. T., et al. 2007, AJ, 134, 102, doi: 10.1086/518474

—. 2008, VizieR Online Data Catalog, 7252

Schneider, D. P., Richards, G. T., Hall, P. B., et al. 2010, AJ, 139, 2360, doi: 10.1088/0004-6256/139/6/2360

Sesar, B., Ivezić, Ž., Lupton, R. H., et al. 2007, AJ, 134, 2236

Shakura, N. I., & Sunyaev, R. A. 1973, A&A, 24, 337

Shen, Y., Greene, J. E., Strauss, M. A., Richards, G. T., & Schneider, D. P. 2008, ApJ, 680, 169, doi: 10.1086/587475

Shen, Y., & Ho, L. C. 2014, Nature, 513, 210, doi: 10.1038/nature13712

Shen, Y., Richards, G. T., Strauss, M. A., et al. 2011, ApJS, 194, 45, doi: 10.1088/0067-0049/194/2/45

Shen, Y., Hall, P. B., Horne, K., et al. 2018, arXiv e-prints, arXiv:1810.01447. https://arxiv.org/abs/1810.01447

Simm, T., Salvato, M., Saglia, R., et al. 2016, A&A, 585, A129, doi: 10.1051/0004-6361/201527353

Smith, K. L., Mushotzky, R. F., Boyd, P. T., et al. 2018, ApJ, 857, 141, doi: 10.3847/1538-4357/aab88d

Śniegowska, M., & Czerny, B. 2019, arXiv e-prints, arXiv:1904.06767. https://arxiv.org/abs/1904.06767

Stern, D., McKernan, B., Graham, M. J., et al. 2018, ApJ, 864, 27, doi: 10.3847/1538-4357/aac726

Sun, J., & Shen, Y. 2015, ApJL, 804, L15, doi: 10.1088/2041-8205/804/1/L15

Sun, M., Xue, Y., Wang, J., Cai, Z., & Guo, H. 2018, ApJ, 866, 74, doi: 10.3847/1538-4357/aae208

Tonry, J. L., Stubbs, C. W., Lykke, K. R., et al. 2012, ApJ, 750, 99, doi: 10.1088/0004-637X/750/2/99

Vanden Berk, D. E., Richards, G. T., Bauer, A., et al. 2001, AJ, 122, 549, doi: 10.1086/321167

Vestergaard, M. 2002, ApJ, 571, 733, doi: 10.1086/340045

Vestergaard, M., & Peterson, B. M. 2006, ApJ, 641, 689, doi: 10.1086/500572

Wang, T., Brinkmann, W., & Bergeron, J. 1996, A&A, 309, 81

Wisotzki, L. 2000, A&A, 353, 861

Yang, J., Fan, X., Wu, X.-B., et al. 2017, AJ, 153, 184, doi: 10.3847/1538-3881/aa6577

Zhu, F.-F., Wang, J.-X., Cai, Z.-Y., et al. 2018, The Astrophysical Journal, 860, 29, doi: 10.3847/1538-4357/aac2d7

Zu, Y., Kochanek, C. S., Kozłowski, S., & Udalski, A. 2013, ApJ, 765, 106, doi: 10.1088/0004-637X/765/2/106

Zu, Y., Kochanek, C. S., & Peterson, B. M. 2011, ApJ, 735, 80